POLITECNICO DI TORINO
Repository ISTITUZIONALE

Microstructural characterization and in vitro bioactivity of porous glass-ceramic scaffolds for bone regeneration by synchrotron radiation X-ray microtomography

(Article begins on next page)

02 September 2025

Microstructural characterization and *in vitro* bioactivity of porous glass-ceramic scaffolds for bone regeneration by synchrotron radiation X-ray microtomography

Chiara Renghini[a,b], Alessandra Giuliani[b], Serena Mazzoni[b], Francesco Brun[c,d], Emanuel Larsson[c,d],

Francesco Baino[e,*], Chiara Vitale-Brovarone[e]

[a] *SOMACIS S.p.A., R&D Department, Via Jesina 17, 60022 Castelfidardo, Italy.*

[b] *Dipartimento di Scienze Cliniche Specialistiche e Odontostomatologiche – Sezione di Biochimica, Biologia e Fisica, Università Politecnica delle Marche, Via Brecce Bianche 1, 60131 Ancona, Italy.*

[c] *Sincrotrone Trieste S.C.p.A, Strada Statale 14 - km 163.5 in AREA Science Park, 34149 Basovizza (Trieste), Italy.*

[d] *Dipartimento di Ingegneria e Architettura, Università degli Studi di Trieste, Via A. Valerio, 10 – 34127 Trieste, Italy.*

[e] *Institute of Materials Engineering and Physics, Applied Science and Technology Department (DISAT), Politecnico di Torino, Corso Duca degli Abruzzi 24, 10129 Torino, Italy.*

* Corresponding author: Francesco Baino

Tel.: +39 011 090 4668

Fax: +39 011 090 4699

E-mail address: francesco.baino@polito.it

Abstract

One of the key purposes of bone tissue engineering is the development of new biomaterials that can stimulate the body's own regenerative mechanism for patient's anatomical and functional recovery. Bioactive glasses, due to their versatile properties, are excellent candidates to fabricate porous 3-D architectures for bone replacement. In this work, morphological and structural investigations are carried out on Bioglass®- and CEL2-derived scaffolds produced by sponge replication (CEL2 is an experimental glass developed at Politecnico di Torino). Synchrotron radiation X-ray microtomography is used to study the samples 3-D architecture, pores size, shape, distribution and interconnectivity, as well as the growth kinetics on scaffolds struts of a newly formed apatitic phase during *in vitro* treatment in simulated body fluid, in order to describe from a quantitative viewpoint the bioactive potential of the analyzed biomaterials. An accurate comparison between architectural features and bioactive behaviour of Bioglass®- and CEL2-derived scaffolds is presented and discussed.

Keywords: X-ray microtomography; Glass-ceramic scaffold; Sponge replication; *In vitro* bioactivity; Bone tissue engineering.

1. Introduction

Tissue engineering has emerged as a promising approach for the repair and regeneration of tissues and organs that are lost, damaged or in general functionally compromised as a results of trauma, injury, disease or aging [1,2].

A key component of tissue engineering approach to bone regeneration is represented by natural or man-made scaffold that acts as a template for cells interactions and formation of bone extracellular matrix providing structural support to the newly formed tissue [3]. An ideal scaffold should fulfil a complex set of characteristics; in summary, it should (i) be three-dimensional (3-D) and highly porous with an interconnected pore network for allowing cells migration and growth as well as flow transport of nutrients and metabolic waste; (ii) be biocompatible and preferably bioresorbable with a controllable resorption rate matching that of bone repair; (iii) exhibit a surface chemistry suitable for cells attachment, proliferation and differentiation; (iv) have mechanical properties comparable to those of the tissues at the site of implantation; (v) have the potential to be commercially produced and safely sterilized without any alteration of its properties [3-5].

Bioactive glasses and glass-ceramics are attractive scaffold materials for bone repair because of their unique abilities to enhance bone formation and to bond to surrounding tissue [6,7]: upon implantation, bioactive glasses, on their surface layers, gradually convert to hydroxyapatite (HA) [8], the main mineral phase of bone, and exhibit osteoconductive as well as osteoinductive properties. Since the discovery of Bioglass® in 1969 [8], bioactive glasses have represented an increasingly great potential for tissue engineering applications, mainly related (but not limited to) the field of bone regeneration. The study of the effects induced by the ions released from bioactive glasses on cells metabolism and genetic response [9], as well as on angiogenesis [10], is one of the research topics attracting utmost interest of researchers.

The increasing attention of the scientific community towards the design and processing of bioactive glass-based scaffolds for tissue regeneration and in-growth is demonstrated by the publication, in

the last three years, of four comprehensive review articles on this topic [11-14]. Several methods have been used to produce inorganic 3-D glass-based scaffolds, including polymer foam replication [15-17], organic pore former burning-out [18,19], selective laser sintering [20] and sol-gel foaming [21]. In particular the polymer foam replication method, first proposed in the 1960s to produce macroporous ceramics of industrial interest [22], has been more recently and very successfully adopted to create porous glass-derived scaffolds closely mimicking the 3-D architecture of dry human trabecular bone [12,15-17].

X-ray computed microtomography (micro-CT) is a powerful tool for scaffold characterisation. Unlike many other techniques for pores shape, size and distribution assessment, such as scanning electron microscopy (SEM) and mercury intrusion porosimetry, micro-CT can non-destructively obtain a 3-D image of a scaffold [23-25]. When combined with 3-D image analysis techniques, micro-CT can therefore provide not only qualitative but also quantitative information on the scaffold structure [26,27]; tissue in-growth can be also imaged, monitored and related to pores morphology after scaffold implantation *in vivo* [28].

The ability of micro-CT to image 3-D structures in a non-destructive way has made its use and application extremely popular across several disciplines including physics, materials science, medicine, mineral processing and powder technology. In addition, the availability of synchrotron radiation X-ray sources has further stimulated the application of micro-CT due to its numerous advantages with respect to conventional X-ray sources, including higher beam intensity, higher spatial coherence and monochromaticity. This work exploits mainly the monochromaticity property of synchrotron radiation because it reduces significantly the beam hardening effects, thus allowing easing the segmentation step of the whole image analysis process.

In the present study, synchrotron radiation X-ray micro-CT was used to analyze the 3-D porous architecture and microstructure of Bioglass[®]- and CEL2-derived scaffolds before and after *in vitro* tests; Bioglass[®] is the commercial name of Hench's 45S5 glass, whereas CEL2 is an experimental silica-based bioactive glass originally developed by the authors at Politecnico di Torino [29,30].

CEL2 composition was tailored with the goal of avoiding large pH changes after contact with biological fluids by giving the glass a lower monovalent oxide content (below 20 mol.%) and slightly higher P_2O_5 content (6 mol.%) compared to commercial 45S5 Bioglass[®] [30]. Although micro-CT studies on bioactive porous glasses have been reported in the last years in the literature [31-34], to the best of the authors' knowledge no micro-CT investigation on Bioglass[®]-derived scaffolds obtained by sponge replication has been documented up to now. In this research work micro-CT was used to analyze in detail the scaffold original 3-D structure in terms of pores size, struts thickness and degree of pore interconnectivity, as well as the 3-D distribution of the newly formed apatitic phase on scaffold walls and its evolution as a function of the soaking time in simulated body fluid (SBF). Furthermore, a comparison between architectural features and bioactive behaviour of Bioglass[®]- and CEL2-derived scaffolds is presented and discussed, in order to confirm and extend the promising results of previous studies [17,29,30,35-39] about the suitability of CEL2 as effective biomaterial for scaffolding.

2. Materials and methods

2.1. Scaffolds preparation

Two melt-derived glasses of different composition were used as starting materials for producing 3-D scaffolds by sponge replication method.

The molar compositions of glasses are reported in Table 1 and correspond to Hench's 45S5 bioactive glass (designated in this work as BG), well known in the biomedical field since the early 1970s and currently sold worldwide under the commercial name of Bioglass[®] [8], and CEL2, an experimental silicate glass that has been originally developed and studied by Vitale-Brovarone and co-workers at Politecnico di Torino since the mid 2000s [17,29,30]. The glasses were prepared by melting the required quantities of raw products (high-purity reagents purchased from Sigma-

Aldrich) in a platinum crucible in air (melting conditions are reported in Table 1). The melt was then quenched into cold water to obtain a "frit" that was ground by using a 6-ball zirconia mill, and the glass powders were eventually sieved through stainless steel sieves to obtain particles with size below 32 μm to be used for scaffolds fabrication.

Sponge replication was chosen for making scaffolds due to its excellent suitability to obtain porous bioceramics with trabecular architecture closely mimicking that of cancellous bone [12]. The processing schedule adopted in this work was extensively described elsewhere [17]. Briefly, cubic blocks ($15.0 \times 15.0 \times 15.0$ mm^3) of commercial polyurethane (PU) sponge were coated with glass powder by impregnating them in a water-based glass slurry (weight composition: 30% glass, 64% distilled water, 6% poly(vinyl alcohol) (PVA)); after PVA dissolution under continuous magnetic stirring at 80 °C, the glass powder was added to the solution. The water evaporated during PVA dissolution was re-added to the slurry and, after further stirring for 0.5 h at room temperature to ensure homogeneity of the slurry, the sponge blocks were immersed for 60 s in the slurry. The slurry infiltrated the porous network of the polymeric templates, which were extracted from the slurry and eventually compressed (20 kPa for 1 s) up to 60% in thickness along the three spatial directions in order to homogeneously remove the exceeding slurry. This infiltration/compression cycle was repeated for three times; after that, a final cycle of impregnation alone without compression was performed. The samples were dried (first at room temperature for 3 h and then in an oven at 70 °C for 3 h) and afterwards thermally treated in order to remove the polymeric template and to sinter the inorganic one; specifically, BG- and CEL2-derived scaffolds were obtained by sintering for 3 h at 1180 and 1000 °C, respectively (heating rate from room temperature to the sintering one: 5 °C min^{-1} in both cases).

2.2. Scaffolds characterization

6

The scaffolds, ground in powders by means of a 1-ball milling machine, underwent wide-angle X-ray diffraction (WA-XRD; 2θ in the 10-70° range) to assess the presence of crystalline phases nucleated during the thermal treatment of sintering. The analysis was performed by using a X'Pert diffractometer (Philips) operating at 40 kV and 30 mA with Bragg-Brentano camera geometry, Cu $K\alpha$ incident radiation, incident wavelength $\lambda = 1.5405$ Å, step size $\Delta(2\theta) = 0.02°$ and fixed counting time of 1 s per step. Crystalline phases were identified by using X'Pert HighScore program equipped with PCPDFWIN database.

Scaffolds *in vitro* bioactivity was assessed by soaking $10 \times 10 \times 10$ mm^3 samples in acellular simulated body fluid (SBF) prepared according to the recipe proposed by Kokubo and Takadama [40]. The scaffolds were immersed in 30 ml of SBF contained in clean polyethylene bottles, that were then placed in an incubator at a controlled temperature of 37 °C (human body temperature); experimental time points were fixed at 14 days and 28 days of treatment in SBF. As commonly done in this kind of experiments [15,17], SBF was replaced every 48 h to simulate fluid circulation in the human body as the cations concentration in the solution progressively decreased during the course of the experiment as a result of changes in the samples surface chemistry. At the end of the experiments, the samples of each scaffolds batch were extracted from SBF, gently rinsed in distilled water and left to dry at room temperature.

Before and after *in vitro* tests in SBF, the scaffolds were silver-coated and their morphology and porous architecture was investigated by scanning electron microscopy (SEM, Philips 525 M; accelerating voltage 15 kV). Energy dispersive spectroscopy (EDS; Philips Edax 9100) was used to investigate the compositional modification occurred on scaffolds surface after soaking in SBF.

2.3. Microstructural analysis by X-ray micro-CT

BG- and CEL2-derived scaffolds underwent advanced microstructural characterization before and after *in vitro* tests to investigate any morphological and architectural changes due to soaking in

SBF. Measurements were carried out on the samples for each time point, i.e. scaffolds as-such, scaffolds soaked in SBF for 14 days (2 weeks) and scaffolds treated in SBF for 28 days (4 weeks).

2.3.1. Experimental set-up

Micro-CT experiments were performed at the SYRMEP beamline of the ELETTRA Synchrotron Radiation Facility (Trieste, Italy). The experimental conditions were selected, according to the properties of the samples. For this experiment, three cubic samples with a side of 5 mm were prepared with the two selected glasses. Due to the sample composition, the energy of the monochromatic beam was set to 27 keV with a sample-to-detector distance of 5 cm; the resulting voxel size was $9 \times 9 \times 9$ μm^3 (i.e., the best resolution obtainable with the adopted setup). The reconstruction of the tomographic slices was carried out using a custom-developed software [41] applying the standard filtered back-projection algorithm [42]. The exposure time was set to 14 s per projection. A total of 900 radiographic images were recorded for each sample, yielding a total scan duration about 215 min.

2.3.2. Image segmentation and extraction of quantitative parameters

The volume data obtained in absorption configuration was analyzed by using the software VG Studio MAX 1.2 and the Pore3D software [43]. Quantitative parameters were calculated directly from 3-D images to characterize the scaffold before and after soaking in SBF. This quantification first required segmenting the different phases to separate them from the background; a 3-D median smoothing filter (kernel width = 3) was applied in order to facilitate segmentation. In the samples before immersion in SBF, such segmentation was easily performed by simple thresholding because the gray level histogram was clearly bimodal with a first peak corresponding to background (air) and a second peak corresponding to scaffold; after *in vitro* tests, however, an intermediated peak related to a newly formed phase appeared (as discussed in the section 3.2., this new phase formed on scaffolds struts will be identified as apatite). The thresholds of segmentation of the gray levels

distribution (0-255 range) were selected according to a method described elsewhere by the authors [35]; representative threshold values were manually set to 85 (apatite) and 128 (scaffold) for the BG-derived sample, and to 94 (apatite) and 149 (scaffold) for the CEL2-derived sample.

Representative volumes of interest (VOIs) of $2.7 \times 2.7 \times 2.7$ mm^3 containing the scaffolds were chosen far away from sample edges. The obtained VOIs were then analyzed, based on the structural indices usually measured for bone samples [44]. The sample volume (SV) is computed by multiplying the number of voxels corresponding to the scaffold material by the voxel size. The total volume (TV) is the VOI, i.e. the number of voxels (normalized taking into account the voxel size) of the sub-volume considered for the analysis. Sample porosity PoreV (vol.%) can therefore be calculated as $(1 - SV/TV)$. The ratio between sample surface (SS) and sample volume (SV), namely SS/SV, is approximated using the Cauchy-Crofton theorem from differential geometry [45].

The apatite volume was also directly measured from the 3-D image stacks. The apatite mean thickness was then calculated using a plate-model assumption in the 3-D analysis software VGStudio Max (v1.2, Volume Graphics, Heidelberg, Germany).

The whole struts thickness distribution was measured using a module of VG Studio MAX 1.2, namely the "Wall thickness analysis" module [46]; the same method was applied to the inverted histogram of the grey levels to quantify the pore thickness distribution.

Anisotropic measurements of the scaffolds, i.e. the presence of preferential orientations, were performed using the mean intercept length (MIL) method. The basic principle of the MIL method is to count the number of intersections between a linear grid and the pore/material interface as a function of the grid orientation ω [47]. The mean intercept length (an intercept is the line between two intersections) is calculated as the ratio between the total length L of the line grid and the number of intersections. MIL measurements in 3-D may be fitted to an ellipsoid which can be expressed as the quadratic form of a second rank tensor M [48]. A fabric tensor H is the defined as the inverse square root of M [49,50]. Since the eigenvectors (u_1, u_2, u_3) of the fabric tensor H give information about the direction of the axes of the ellipsoid, and the eigenvalues (t_1, t_2, t_3) express the

radii of the ellipsoid, the latter can be used to define the degree of anisotropy, which denotes the ratio between the maximal and minimal radii of the MIL. In this article, the eigenvalues are summarized using the isotropy index $I = t_3/t_1$ and the elongation index $E = 1 - t_2/t_1$ [51]. The isotropy index I measures the similarity of a fabric to a uniform distribution and varies between 0 (all observation confined to a single plane or axis) and 1 (perfect isotropy). The elongation index measures the preferred orientation of a fabric in the $[u_1, u_2]$ plane and varies between 0 (no preferred orientation) and 1 (a perfect preferred orientation with only parallel observations).

Provided that the scaffold is a connected structure with no closed void cavities, a simple indicator of the connectedness of the 3-D complex pore space is the Euler number χ_V. For an open network structure, the Euler number may be calculated from the number of nodes n and the number of branches b after skeletonization of the pore space as $\chi_V = n - b$ [47]. It provides a measure of connectivity indicating the number of redundant connections: the breaking of a single connection will leave the network less connected increasing the value of χ_V, while the addition of a redundant connection will decrease it [52]. In order to normalize the Euler number with respect to the size of the considered volume V, the parameter "connectivity density" β computed as $\beta = (1 - \chi_V)/V$ is commonly adopted [52]. The connectivity density does not carry information about positions or size of connections but it is a simple global measure of connectivity, which gives higher values for better-connected structures, and lower values for poorly connected structures. In the present work, interconnectivity was measured using an algorithm implemented in Pore3D, namely gradient vector flow (GVF) [53], which performs the connectivity analysis in 3-D [54,55].

3. Results and discussion

3.1. Analysis of the scaffolds before treatment in SBF

3.1.1. Scaffolds materials

10

WA-XRD performed on as-poured BG and CEL2 powders (Figs. 1a,c) revealed that both starting materials are amorphous since only a broad halo in the 25-38° 2θ-range is visible in the diffraction patterns, as shown by similar analyses reported elsewhere [17,56]. Sintered scaffolds ground in powders also underwent WA-XRD; the resulting diffraction spectra are reported in Figs. 1b,d. As demonstrated from the well-distinguishable peaks visible in the plots, BG- and CEL2-derived scaffolds are both constituted by glass-ceramic materials, hereafter designed as GC-BG and GC-CEL2, respectively.

$Na_2CaSi_2O_6$ and $Na_2Ca_4(PO_4)_2SiO_4$ were identified, respectively, as the major and the secondary crystalline phase of GC-BG (Fig 1b), in good accordance with previous observations by the authors [56] as well as with the results by other research groups [57,58]. It is interesting to mention that $Na_2Ca_2Si_3O_9$ is often suggested in the literature for an alternative identification of the main crystalline phase in sintered Bioglass® [15,59,60]; in the attempt at solving such a controversy, coexistence of $Na_2CaSi_2O_6$ and $Na_2Ca_2Si_3O_9$ has been recently proposed [61] also in the light of the marked overlapping of the XRD peaks corresponding to these two phases.

Fig. 1d reveals the presence of two crystalline phases, $Na_4Ca_4(Si_6O_{18})$ and $Ca_2Mg(Si_2O_7)$, in GC-CEL2 scaffolds, as assessed elsewhere by the authors [17].

3.1.2. Architecture and morphology

Fig. 2 shows the typical surface and cross-sectional appearance of the analyzed scaffolds. As evident from Figs. 2a,b, the sintered scaffolds closely mimic the peculiar pores/struts architecture of the starting open-cell polymeric template, that is very similar to the trabecular porous organization of cancellous bone, characterized by relevant pores interconnectivity. Figs. 2c,d shows that the size of the large macropores of scaffolds is well above 100 μm, which is strongly recommended for bone tissue engineering scaffolds in order to allow bone cells migration and colonization into the porous implant as well as its vascularisation [3].

11

A 3-D volume rendering and 2-D axial slices from the 3-D micro-CT images of GC-BG and GC-CEL2 scaffolds were illustrated in Fig. 3. The images allow appreciating the bone-like structure of both types of scaffolds. The pores are interconnected and characterized by a quite irregular shape, which makes them more similar to those of cancellous bone in comparison with, for instance, the perfectly spherical pores of bioactive glass scaffolds obtained by sol-gel foaming [31,32]. In both type of scaffolds, however, the struts are generally thicker than those typical of natural spongy bone, in which the pores are so open that it is difficult to distinguish what can be considered a pore from what is actually a pore window [25].

The total porosity and the SS/SV ratio are summarized in Table 2. It is interesting to notice that GC-BG scaffolds were found to be more porous (~63 vol.%) than the GC-CEL2 ones (~40 vol.%) although they were obtained from an identical polymeric sponge. This finding can be explained by taking into account the different sinterability of the two glasses, which ensues in different densification of the struts as well as mechanical strength [56].

Especially for CEL2-derived scaffolds, the total pores content assessed by micro-CT analysis is lower than that evaluated by weight-volume measurements performed elsewhere [17]; this difference can be explained considering that the nanopores as well as the smallest micrometric pores are not detected by micro-CT due to the resolution limit of the instrument. This underestimation of porosity was already observed by the authors in the case of other batches of CEL2-derived foam-like scaffolds described elsewhere [29,35].

Being the morphology of GC-BG and GC-CEL2 scaffolds very heterogeneous, as shown in Fig. 3, mean morphometric parameters do not correctly represent the strut thickness and the pore size distribution of the whole samples: therefore, the 3-D images were also quantified by using computational techniques. Fig. 4 shows 3-D maps of the wall thickness distribution (Figs. 4a,b) and of the pore size distribution (Figs. 4c,d) of the analysed GC-BG and GC-CEL2 scaffolds, where different strut thicknesses/pore size are plotted with different colours. The distributions of wall thickness and pore size of the 3-D microstructures were also quantitatively assessed: the histograms

of dimensional distribution computed for these two parameters are plotted in Figs. 4e,f. Fig. 4f quantitatively confirms that most of pores of both scaffolds is in the 100-700 μm range, as preliminarily shown in Fig. 2 and Fig. 3, which is a fundamental feature in view of *in vivo* osteointegration of the implant [3].

It is interesting to make a comparison between the architectural features of the GC-CEL2 scaffolds analyzed in the present work and those of the CEL2-derived scaffolds produced by sponge replication method with different processing parameters [29] and investigated by micro-CT in a previous work [35]. The former GC-CEL2 scaffolds exhibited higher pores content (54 vol.%), [35] in comparison to the GC-CEL2 scaffolds described in the present research (Table 2). These different characteristics can be explained considering that the method for scaffolding was purposely optimized and standardised, as described in detail elsewhere [17], in order to produce high-strength GC-CEL2 scaffolds (compressive strength above 5 MPa [17] versus ~1 MPa [29,35]) with thicker struts and lower pores content in comparison with those fabricated previously. From a mechanical viewpoint, GC-CEL2 scaffolds with compressive strength of 5 MPa are very promising candidates for bone grafting, also taking in account that the compressive strength of a scaffold can significantly increase *in vivo* due to tissue in-growth. The cells adherent on scaffold, the newly formed tissue and the scaffold itself create a biocomposite construct *in situ*, thereby increasing the time-dependent scaffold strength.

Porosity and pore size of biomaterial scaffolds play indeed a critical role in bone formation *in vitro* and *in vivo*. In general, large pores typically within 100-700 μm favour direct osteogenesis, since they allow vascularisation and high oxygenation, while smaller pores are useful for osteochondral ossification [3]; however, bone in-growth also depends on the type of used biomaterial as well as on the geometry of the pores. The proposed scaffolds have shown to present a pore diameter distribution in the range of the optimal pore sizes (Fig. 4f) and the pore morphologies (Figs. 3b,d) resemble those of cancellous bone, where trabeculae are irregular in shape and size.

3.2. Analysis of the scaffolds after treatment in SBF

GC-BG and GC-CEL2 scaffolds were soaked in SBF for different time intervals (14 days and 28 days) to investigate their bioactive potential by monitoring the modifications that occurred on their struts during immersion. After the experiments, some samples were embedded in epoxy resin (Struers Epofix), cut by a diamond wheel (Struers Accutom 5), polished by using #600 to #4000 SiC grit papers and finally investigated by SEM; two examples of resulting cross-sections are reported in Figs. 5a,b. The back-scattering mode adopted for SEM analysis emphasizes the presence of a newly formed phase grown on scaffolds walls, as indicated in the picture. Compositional analysis by EDS revealed that this layer is rich in calcium and phosphorus, with a Ca/P molar ratio that increased from 1.5-1.6 after 2 weeks of treatment in SBF to 1.62-1.67 after 4 weeks. These findings are consistent with the reaction stages proposed by Hench and co-workers for describing *in vitro* bioactivity of biomedical SiO_2-based glasses [8], involving the formation of a layer of amorphous calcium phosphate, that progressively evolves into Ca-deficient HA and finally crystallizes in stoichiometric HA (Ca/P = 1.67 mol.). From a microstructural viewpoint, the HA formed on GC-BG and GC-CEL2 scaffolds is constituted by globular agglomerates imparting a "cauliflower" appearance to the layer (Fig. 5c), which is typical of the apatite grown on bioactive glasses.

The presence of an apatitic layer on scaffold struts plays a key role in promoting the graft colonization by bone cells, as it was widely demonstrated that osteoblasts attach preferably on crystals of apatite due to its chemical and crystallographic similarity to bone mineral [6-8,11-14,17,29,30]. By using an evocative image, the apatite layer can be viewed as a "biomimetic skin" making scaffold surface, struts and pores walls a highly biocompatible substrate apt for cells adhesion. The presence of this "apatite coating" on the scaffold is also highly related to the bond-bonding ability of biomaterials *in vivo* [8].

At a preliminary look, the apatite layer formed on GC-CEL2 scaffolds (Fig. 5b) seems to be thicker than that grown on the GC-BG ones (Fig. 5a), which could suggest a higher bioactivity of GC-CEL2 samples. The average thickness of the apatite layer was quantitatively derived by micro-CT image stacks and reported as a function of the immersion time in Fig. 6. As can be seen, in the GC-CEL2 scaffolds with increasing immersion time there was a significant increment in the apatite layer thickness with respect to GC-BG samples. In particular, after 4 weeks the average apatite thickness increased to a value of almost 29 μm for GC-CEL2 scaffolds, whereas the apatite layer thickness of GC-BG samples increased to a value of almost 16 μm after 2 weeks and then remained almost constant without further increment. This effect can be at least partially attributed to the features of the crystalline phases nucleated in sintered Bioglass®, as their influence on bioactivity has been documented in the literature. In the early 1990s Li et al. [62] reported that significant crystallization of Bioglass® turns the bioactive glass into a inert-like material. More recently, this crucial issue was investigated in detail by LaTorre and co-workers [63,64] who showed that the major crystalline phase of sintered Bioglass® decreases the kinetics of formation of apatite on the Bioglass®-derived glass-ceramic, but does not totally suppress the growth of this bioactive layer.

The relationship between glass composition and bioactive behaviour is generally a complex issue, as many factors have to be taken in account. For instance, it was suggested by Watts et al. [65] that MgO would act to decrease the bioactivity of biomedical glasses belonging to the SiO_2-P_2O_5-CaO-MgO-Na_2O system in comparison with 45S5 Bioglass®. In the case of CEL2, however, also K_2O was introduced in the glass formulation; therefore, the first stage of bioactivity of bioactive glass, characterized by monovalent cations exchange [8], would involve not only H^+/Na^+ but also H^+/K^+ exchange phenomena. K^+ has a quite large ionic radius (0.133 nm) in comparison with Na^+ (0.095 nm); therefore, K^+ release would have a high disrupting effect on glass network thereby enhancing CEL2/GC-CEL2 specific surface area and reactivity. Furthermore, Mg is at least partially confined in one of the two crystalline phases of GC-CEL2, i.e. $Ca_2Mg(Si_2O_7)$ [17,56], and therefore only a fraction of it is contained in the residual amorphous phase involved in the bioactivity mechanism;

15

this gives also an explanation of the higher bioactivity of GC-CEL2 with respect to the parent glass CEL2 observed by Miola et al. [66].

The mean thickness of the newly formed apatite layer (Fig. 6), assessed by micro-CT on the whole samples volume, could be therefore assumed, at least ideally, as a first index to quantify and compare the *in vitro* bioactivity of the scaffolds. The bioactivity of GC-CEL2 scaffolds was then found to be significantly higher than that of GC-BG samples, as evident from the difference of thickness of the apatite layer formed on the scaffolds struts at the last time point (4 weeks).

Although the use of micro-CT to obtain quantitative assessments of the bioactivity of biomaterials is fascinating, this approach is often unfeasible in the majority of research contexts, as micro-CT still remains an expensive and not easily accessible technique, and it also takes a long time to carry out a scan as well as to reconstruct and to analyze the images. Considering its great potential, micro-CT should be strongly recommended − if accessible − as a useful complementary technique to conventional bioactivity testing, especially in the case of porous biomaterials.

3-D spatial distribution of the new phase into the analysed scaffolds at 2 and 4 weeks after the immersion in SBF are illustrated in Fig. 7 and Fig. 8. Micro-CT can also give qualitative information on the density of materials; in this case, the newly formed apatitic phase was characterized by lower density than that of the scaffold material [56], as HA is not fully dense due to its "cauliflower" morphology (Fig. 5c). After 4 weeks of treatment in SBF, the newly formed apatite layer is well evident also in the inner regions of the scaffolds (Fig. 7c and Fig. 8c), which demonstrates that the biological fluid can flow between the pores of the scaffold.

Table 2 also shows the measured 3-D morphometric parameters at 2 and 4 weeks of immersion time; the pores size distributions and the struts thickness distribution of the scaffolds before and after treatment in SBF are compared in Fig. 9 and Fig. 10, respectively. After treatment in SBF, all analyzed scaffolds exhibited a pores content ranging from 42 to 49 vol.%; after immersion in SBF for 14 days, the total porosity of GC-BG scaffolds highly decreased while the pores content of GC-CEL2 samples showed an increment (Table 2). Moreover, significant pores enlargement (Fig. 9b)

16

and strut thickening (Fig. 10b) can be noticed in GC-CEL2 scaffolds after immersion; on the contrary, the GC-BG samples showed an important and progressive decrement in pore size (Fig. 9a). Such results suggest that GC-CEL2 scaffolds are more prone to dissolution in SBF (dissolution of the thinnest struts occurs, as demonstrated in Fig. 10b, with subsequent "merging" of small pores in larger ones, as shown in Fig. 9b) than GC-BG samples, which is related to the different bioactivity of the two biomaterials.

Table 3 reports the results of the anisotropy analysis of the scaffolds, with isotropy index values close to 1 (perfect isotropy) and elongation index values close to 0 (no preferred orientation), which confirms that both BG- and CEL2-derived scaffolds are highly isotropic with no preferred orientations before and after immersion in SBF for 14 and 28 days. A small increase in isotropy can also be seen for GC-BG scaffolds when comparing the isotropy index values before and after immersion in SBF for 28 days, whereas the isotropy index for GC-CEL2 scaffolds remains almost unchanged before and after the treatment in SBF for 14 and 28 days. Also the elongation index for both GC-BG and GC-CEL2 scaffolds remains rather unchanged, before and after immersion in SBF for 14 and 28 days.

Table 4 shows the connectivity properties of the two different scaffolds. GC-BG scaffold has a higher connectivity density with respect to the GC-CEL2 one before immersion in SBF. After soaking for 14 days in SBF, GC-BG scaffold connectivity decreases significantly, probably due to the in-growth of the new apatitic phase that fills and "closes" small pores. This hypothesis seems to be also supported by the histogram reported in Fig. 9a: the reduction of the amount of pores below 150 μm in GC-BG scaffolds soaked for 14 days in SBF might be due to pores "clotting" by apatite. After 28 days of immersion in SBF the connectivity density increases again, due to the continuous and progressive dissolution of scaffold material accompanied to the formation of new small pores in the pre-existing scaffold struts (Fig. 9a).

On the basis of the reported analyses, the pores/struts modification occurring in GC-BG scaffolds during immersion in SBF can be therefore resumed as follows. During the early 14 days of soaking

in SBF, GC-BG scaffold struts are progressively coated by an apatite layer, which ensues in a decrement of total pores content, as shown in Table 2. Afterwards, between 14 and 28 days of soaking, scaffold dissolution kinetics become predominant with respect to those of apatite formation: formation of networks of new small pores on and in scaffold struts, according to a sort of "pitting mechanism", involves increase of total pores content (Table 2) due to neo-formation of very small pores (Fig. 9a) separated by very thin trabeculae.

As far as GC-CEL2 samples, we can suppose that the kinetics of apatite formation and scaffold material dissolution are both relevant during the early 14 days of soaking in SBF. In fact, we assist both to increment of total pores content (Table 2), which can be due to GC-CEL2 dissolution in SBF, and to increase of struts thickness, due to dissolution of the thinnest trabeculae (progressive disappearance of the smallest pores, see Fig. 9b) as well as to apatite formation on scaffold struts. GC-CEL2 scaffolds seem to exhibit a higher reactivity in SBF with respect to GC-BG samples, as especially demonstrated by the relevant increase of total porosity (PoreV) after 14 days (Table 2) due to scaffold material dissolution and already observed elsewhere [35]; relevant tendency to dissolution might also be responsible for the increase of connectivity density at 14 days (Table 4). By increasing the soaking time in SBF, apatite formation becomes progressively predominant with respect to scaffold material dissolution, as confirmed by further decrease of total porosity (Table 2) due to continuous apatite formation (see also Fig. 6). A "pore-clotting" effect of the apatite filling small pores might be also present, as suggested by the histograms reported in Fig. 9b showing a progressive reduction of the amount of the pores below 150 μm over immersion time. This effect could also justify the decrease of the connectivity density noticed at 28 days (Table 4): "pore-clotting" might be effective even on pores with dimension up to 300 μm (Fig. 9b), thereby contributing to the increase of mean struts thickness and ensuing in the reduction of the connectivity nodes.

4. Conclusions

In this work, Bioglass®- and CEL2-derived glass-ceramic scaffolds were fabricated through the sponge replication method with the same processing schedule followed by an appropriate sintering treatment. Micro-CT analysis revealed that the 3-D porous architecture of both types of scaffolds closely mimicked that of cancellous bone, with distribution of macropores diameter in the range of the optimal pores size (100-800 μm) recommended for bone tissue engineering scaffolds. The high interconnectivity of scaffolds open macropores is a valuable property expected to allow bone cells migration into the scaffold, bone in-growth and implant vascularisation *in vivo*.

Micro-CT investigations showed that a HA layer progressively grew on samples struts during *in vitro* tests in SBF, which put in evidence the high bioactive properties of the prepared scaffolds. Bioactivity of CEL2-derived scaffolds was found superior to that of Bioglass®-derived ones, as evaluated by the different thickness of the HA layer formed on their struts after 4 weeks in SBF (~29 μm versus ~16 μm); in addition, the apatite layer formed on Bioglass®-based scaffolds showed no further increment in thickness when the soaking time in SBF was increased from 2 to 4 weeks.

CEL2-derived scaffolds, as expected from their higher bioactivity, were also found more prone to dissolution is SBF, which ensued in marked pores enlargement during *in vitro* treatment.

This work confirms that micro-CT technique can play a fundamental role in the advanced characterization of porous biomaterials because it allows, in a non-invasive and non-destructive way, a complete, precise and high-resolution analysis in 3-D of scaffold microstructural parameters. Specifically, micro-CT proved to be a powerful tool to investigate, from a quantitative viewpoint, the bioactive potential of foam-like glass-derived scaffolds, which is a crucial issue in view of their possible clinical use in the future.

Acknowledgements

References

[1] Nerem RM. Cellular engineering. *Ann Biomed Eng* 1991;**19**:529–45.

[2] Langer R, Vacanti JP. Tissue engineering. *Science* 1993;**260**:920–6.

[3] Karageorgiou V, Kaplan D. Porosity of 3-D biomaterial scaffolds and osteogenesis. *Biomaterials* 2005;**26**:5474–91.

[4] Hutmacher DW. Scaffolds in tissue engineering bone and cartilage. *Biomaterials* 2000;**21**:2529–43.

[5] Jones JR, Gentleman E, Polak J. Bioactive glass scaffolds for bone regeneration. *Elements* 2007;**3**:393–9.

[6] Oonishi H, Kushitani S, Yasukawa E, Iwaki H, Hench LL, Wilson J, Tsuji EI, Sugihara T. Particulate bioglass compared with hydroxyapatite as a bone graft substitute. *Clin Orthop Relat Res* 1997;**334**:316–25.

[7] Oonishi H, Hench LL, Wilson J, Sugihara F, Tsuji E, Matsuura M, Kin S, Yamamoto T, Mizokawa S. Quantitative comparison of bone growth behavior in granules of Bioglass® glass-ceramic, and hydroxyapatite. *J Biomed Mater Res* 2000;**51**:37–46.

[8] Hench LL. The story of Bioglass®. *J Mater Sci: Mater Med*, 2006;**17**:967-78.

[9] Hoppe A, Guldal NS, Boccaccini AR. A review of the biological response to ionic dissolution products from bioactive glasses and glass-ceramics. *Biomaterials* 2011;**32**:2757–74.

[10] Gerhardt LC, Widdows KL, Erol MM, Burch CV, Sanz-Herrera JA, Ochoa I, Stampfli R, Roqan IS, Gabe S, Ansari T, Boccaccini AR. The pro-angiogenic properties of multi-functional bioactive glass composite scaffolds. *Biomaterials* 2011;**32**:4096–108.

[11] Gerhardt LC, Boccaccini AR. Bioactive glass and glass-ceramic scaffolds for bone tissue engineering. *Materials* 2010;**3**:3867–910.

[12] Baino F, Vitale-Brovarone C. Three-dimensional glass-derived scaffolds for bone tissue engineering: current trends and forecasts for the future. *J Biomed Mater Res A* 2011;**97**:514–35.

[13] Rahaman MN, Day DE, Bal BS, Fu Q, Jung SB, Bonewald LF, Tomsia AP. Bioactive glass in tissue engineering. *Acta Biomater* 2011;**7**:2355–73.

[14] Fu Q, Saiz E, Rahaman MN, Tomsia AP. Bioactive glass scaffolds for bone tissue engineering: state of the art and future perspectives. *Mater Sci Eng C* 2011;**31**:1245–56.

[15] Chen Q, Thompson ID, Boccaccini AR. 45S5 Bioglass[®]-derived glass-ceramic scaffolds for bone tissue engineering. *Biomaterials* 2006;**27**:2414–25.

[16] Fu Q, Rahaman MN, Bal BS, Brown RF, Day DE. Mechanical and in vitro performance of 13-93 bioactive glass scaffolds prepared by a polymer foam replication technique. *Acta Biomater* 2008;**4**:1854–64.

[17] Vitale-Brovarone C, Baino F, Verné E. High strength bioactive glass-ceramic scaffolds for bone regeneration. *J Mater Sci: Mater Med* 2009;**20**:643–53.

[18] Baino F, Verné E, Vitale-Brovarone, C. 3-D high strength glass-ceramic scaffolds containing fluoroapatite for load-bearing bone portions replacement. *Mater Sci Eng C* 2009;**29**:2055–62.

[19] Wu SC, Hsu HC, Hsiao SH, Ho WF. Preparation of porous 45S5 Bioglass[®]-derived glass-ceramic scaffolds by using rice husk as a porogen additive. *J Mater Sci: Mater Med* 2009;**20**:1229–36.

[20] Kolan KCR, Leu MC, Hilmas GE, Brown RF, Velez M. Fabrication of 13-93 bioactive glass scaffolds for bone tissue engineering usig indirect laser sintering. *Biofabrication* 2011;**3**:025004.

[21] Jones JR, Ehrenfried LM, Hench LL. Optimising bioactive glass scaffolds for bone tissue engineering. *Biomaterials* 2006;**27**:964–73.

[22] Schwarzwalder K, Somers AV. Method of making porous ceramic articles. (1963). US patent 3,090,094.

[23] Stock SR. X-ray microtomography of materials. *Int Mater Rev* 1999;**44**:141–64.

[24] Cancedda R, Cedola A, Giuliani A, Komlev V, Lagomarsino S, Mastrogiacomo M, Peyrin F, Rustichelli F. Bulk and interface investigations of scaffolds and tissue-engineered bones by X-ray microtomography and X-ray microdiffraction. *Biomaterials* 2007;**28**:2505–24.

[25] Stock SR. Recent advances in X-ray microtomography applied to materials. *Int Mater Rev* 2008;**53**:129–81.

[26] Atwood RC, Jones JR, Lee PD, Hench LL. Analysis of pore interconnectivity in bioactive glass foams using X-ray microtomography. *Scripta Mater* 2004;**51**:1029–33.

[27] Konerding MA. Scanning electron-microscopy of corrosion casting in medicine. *Scanning Microsc* 1991;**5**:851–65.

[28] Jones AC, Arns CH, Hutmacher DW, Milthorpe BK, Sheppard AP, Knackstedt MA. The correlation of pore morphology, interconnectivity and physical properties of 3D ceramic scaffolds with bone ingrowth. *Biomaterials* 2009;**30**:1440–51.

[29] Vitale-Brovarone C, Verné E, Robiglio L, Appendino P, Bassi F, Martinasso G, Muzio G, Canuto R. Development of glass-ceramic scaffolds for bone tissue engineering: Characterisation, proliferation of human osteoblasts and nodule formation. *Acta Biomater* 2007;**3**:199–208.

[30] Vitale-Brovarone C, Verné E, Robiglio L, Martinasso G, Canuto RA, Muzio G. Biocompatible glass-ceramic materials for bone substitution. *J Mater Sci: Mater Med* 2008;**19**:471–8.

[31] Jones JR, Poologasundarampillai G, Atwood RC, Bernard D, Lee PD. Non-destructive quantitative 3D analysis for the optimisation of tissue scaffolds. *Biomaterials* 2007;**28**:1404–13.

[32] Jones JR, Atwood RC, Poologasundarampillai G, Yue S, Lee PD. Quantifying the 3D macrostructure of tissue scaffolds. *J Mater Sci: Mater Med* 2009;**20**:463–71.

[33] Yue S, Lee PD, Poologasundarampillai G, Yao ZZ, Rockett P, Devlin AH, Mitchell CA, Konerding, MA, Jones JR. Synchrotron X-ray microtomography for assessment of bone tissue scaffolds. *J Mater Sci: Mater Med* 2010;**21**:847–53.

[34] Yue S, Lee PD, Poologasundarampillai G, Jones JR. Evaluation of 3-D bioactive glass scaffolds dissolution in a perfusion flow system with X-ray microtomography. *Acta Biomater* 2011;**7**:2637–43.

[35] Renghini C, Komlev V, Fiori F, Vernè E, Baino F, Vitale-Brovarone C. Micro-CT studies on 3-D bioactive glass–ceramic scaffolds for bone regeneration. *Acta Biomater* 2009;**5**:1328–37.

[36] Baino F, Verné E, Vitale-Brovarone C. Feasibility, tailoring and properties of polyurethane/bioactive glass composite scaffolds for tissue engineering. *J Mater Sci: Mater Med* 2009;**20**:2189–95.

[37] Vitale-Brovarone C, Baino F, Bretcanu O, Verné E. Foam-like scaffolds for bone tissue engineering based on a novel couple of silicate-phosphate specular glasses: synthesis and properties. *J Mater Sci: Mater Med* 2009;**20**:2197–205.

[38] Muzio G, Verné E, Canuto RA, Martinasso G, Saracino S, Baino F, Miola M, Berta L, Frairia R, Vitale-Brovarone C. Shock waves induce activity of human osteoblast-like cells in bioactive scaffolds. *J Trauma Injury Infection Crit Care* 2010;**68**:1439–44.

[39] Vitale-Brovarone C, Baino F, Verné E. Feasibility and tailoring of bioactive glass-ceramic scaffolds with gradient of porosity for bone grafting. *J Biomater Appl* 2010;**24**:693–712.

[40] Kokubo T, Takadama H. How useful is SBF in predicting in vivo bone bioactivity?. *Biomaterials* 2006;**27**:2907–15.

[41] Montanari F. SYRMEP TOMO PROJECT tutorial. Internet report, Sincrotrone Trieste; 2003.

[42] Kak A.C., Slaney M. Principles of computerized tomographic imaging. Society of Industrial and Applied Mathematics 2001. Originally published by IEEE Press at http://www.slaney.org/pct/pct-toc.html.

[43] Brun F, Mancini L, Kasae P, Favretto S, Dreossi D, Tromba G. Pore3D: a software library for quantitative analysis of porous media. *Nucl Instr Methods Phys Res A* 2010;**615**:326–32.

[44] Ulrich D, Van Rietbergen B, Laib A, Ruegsegger P. Load transfer analysis of the distal radius from in-vivo high-resolution CT-imaging. *J Biomech* 1999;**32**:821–8.

[45] Parfitt AM. Bone histomorphometry: standardization of nomenclature, symbols, and units. Report of the ASBMR Histomorphometry Nomenclature Committee; 1987.

[46] http://www.volumegraphics.com/en/products/vgstudio-max.html

[47] Whitehouse WJ. The quantitative morphology of anisotropic trabecular bone. *J Microsc* 1974;**101**:153–68.

[48] Harrigan TP, Mann RW. Characterization of microstructural anisotropy in orthotropic materials using a second rank tensor. *J Mater Sci* 1984;**19**:761–7.

[49] Cowin SC, Laborde AJ The relationship between the elasticity tensor and the fabric tensor. *Mech Mater* 1985;**4**:137–47.

[50] Cowin SC. Wolff's law of trabecular architecture at remodeling equilibrium. *J Biomech Eng* 1986;**108**:83–8.

[51] Odgaard A, Gundersen HJ. Quantification of connectivity in cancellous bone, with special emphasis on 3-D reconstructions. *Bone* 1993;**14**:173–82.

[52] Benn DI. Fabric shape and the interpolation of sedimentary fabric data. *J Sediment Res* 1994;64:910–5.

[53] Xingen W, Spencer SA, Shen S, Fiveash JB, Duan J, Brezovich IA. Development of an accelerated gvf semiautomatic contouring algorithm for radiotherapy treatment planning. *Computers Biol Med* 2009;**39**:650–6.

[54] Brun F, Dreossi D. Efficient curve-skeleton computation for the analysis of biomedical 3D images. *Biomed Sci Instr* 2010;**46**:475-80.

[55] Ketcham RA, Ryan TM. Quantification and visualization of anisotropy in trabecular bone. *J Microsc* 2004;**213**:158–71.

[56] Baino F, Ferraris M, Bretcanu O, Verné E, Vitale-Brovarone C. Optimization of composition, structure and mechanical strength of bioactive 3-D glass-ceramic scaffolds for bone substitution. *J Biomater Appl* (in press) DOI: 10.1177/0885328211429193

[57] Lefebvre L, Chevalier J, Gremillard L, Zenati R, Thollet G, Bernache-Assolant D, Govin A. Structural transformation of bioactive glass 45S5 with thermal treatments. *Acta Mater* 2007;**55**:3305–13.

[58] Lefebvre L, Gremillard L, Chevalier J, Zenati R, Bernache-Assolant D. Sintering behaviour of 45S5 bioactive glass. *Acta Biomater* 2008;**4**:1894–903.

[59] Peitl FO, LaTorre GP, Hench LL. Effect of crystallization on apatite-layer formation of bioactive glass 45S5. *J Biomed Mater Res* 1996;**30**:509–14

[60] Bretcanu O, Chatzistavrou X, Paraskevpoulos K, Conradt R, Thompson I, Boccaccini AR. Sintering and crystallization of 45S5 Bioglass® powder. *J Eur Ceram Soc* 2009;**29**:3299–306.

[61] Bellucci D, Cannillo V, Sola A, Chiellini F, Gazzarri M, Migone C. Macroporous Bioglass®-derived scaffolds for bone tissue regeneration. *Ceram Int* 2011;**37**:1575–85.

[62] Li P, Zhang F, Kokubo T. The effect of residual glassy phase in a bioactive glass-ceramic on the formation of its surface apatite layer in vitro *J Mater Sci: Mater Med* 1992;**3**:452–6.

[63] Peitl FO, LaTorre GP, Hench LL. Effect of crystallization on apatite-layer formation of bioactive glass 45S5. *J Biomed Mater Res* 1996;**30**:509–14.

[64] Clupper DC, Mecholsky JJ Jr., LaTorre GP, Greenspan DC. Bioactivity of tape cast and sintered glass-ceramic in simulated body fluid. *Biomaterials* 2002;**23**:2599–606.

[65] Watts SJ, Hill RG, O'Donnell MD, Law RV. Influence of magnesia on the structure and properties of bioactive glasses. *J Non-Cryst Solids* 2010;**356**:517–24.

[66] Miola M, Vitale-Brovarone C, Mattu C, Verné E. Antibiotic loading on bioactive glasses and glass-ceramics: an approach to surface modification. *J Biomater Appl* (in press) DOI: 10.1177/0885328212447665

Figure

Fig. 1. XRD patterns of (a) as-poured BG, (b) BG-derived scaffold (sintering conditions: 1180 °C/3h) after grinding in powder, (c) as-poured CEL2, (d) CEL2-derived scaffold (sintering conditions: 1000 °C/3h) after grinding in powder.
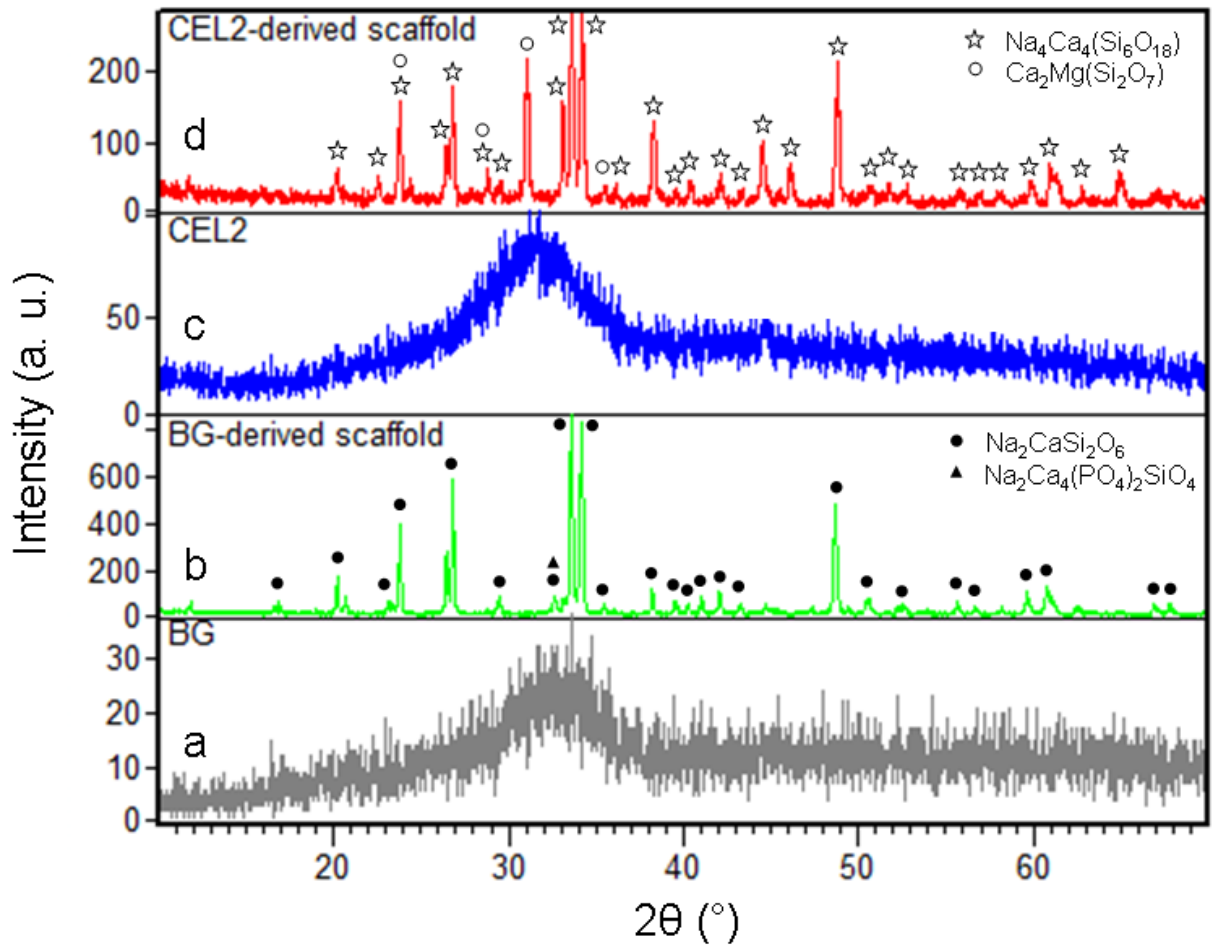
Fig. 2. Morphology of the samples investigated by SEM: surface of (a) GC-BG and (b) GC-CEL2 cubic scaffolds (magnification 50× in both cases); cross-section of (c) GC-BG and (d) GC-CEL2 scaffolds (magnification 80× in both cases). In (c) the pores of GC-BG scaffold, analyzed in back-scattering mode, are filled by the epoxy resin in which the sample was embedded before cutting.
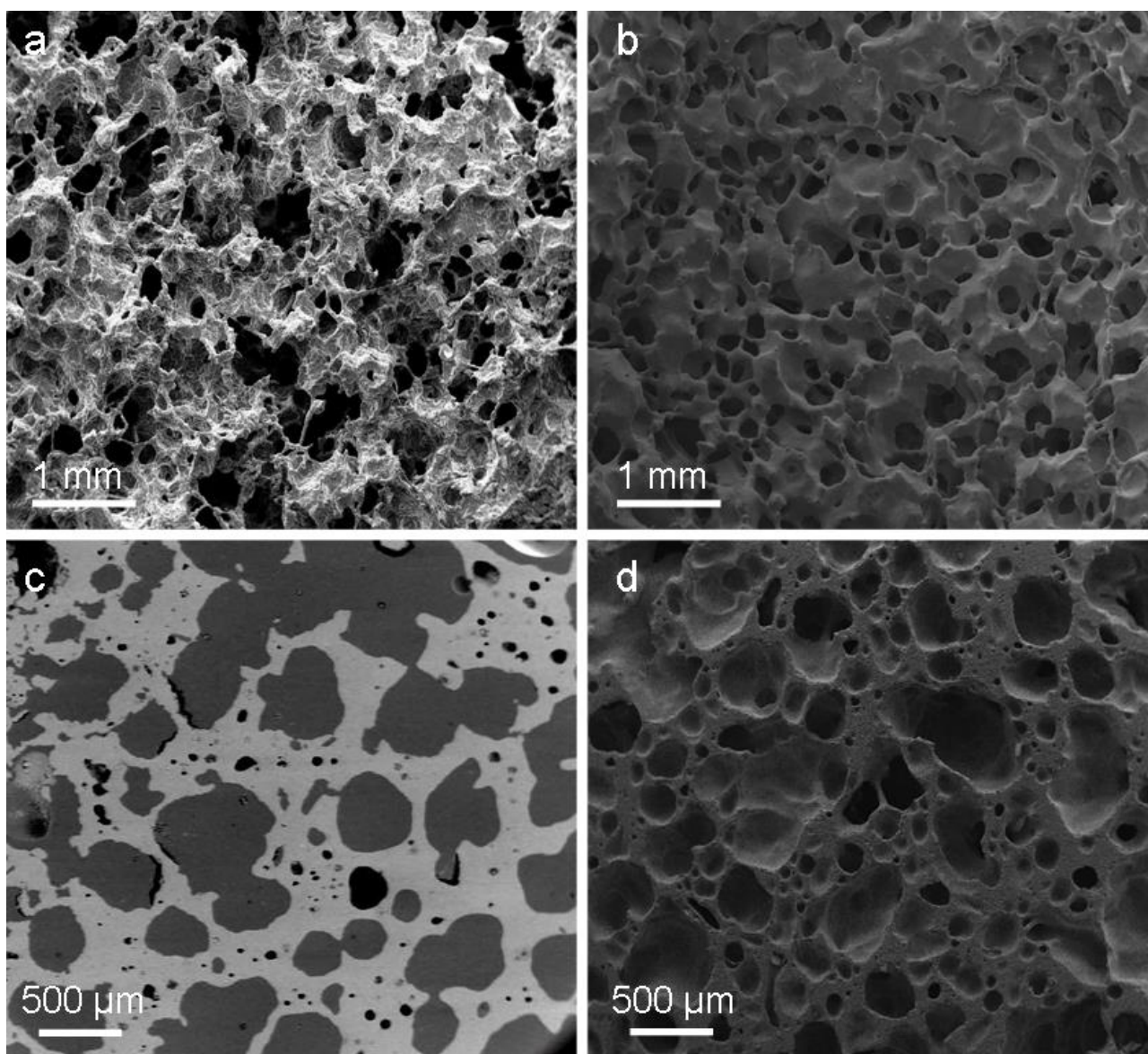
Fig. 3. Micro-CT analyses of the scaffolds as-such (before SBF): 3-D reconstructions of cubic subvolumes (VOI: $2.7 \times 2.7 \times 2.7$ mm^3) of (a) GC-BG and (c) GC-CEL2 scaffolds; 2-D slices of the same VOIs of (b) GC-BG and (d) GC-CEL2 scaffolds.
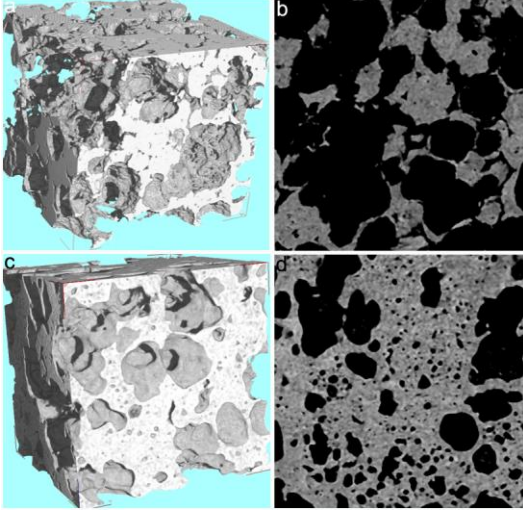

Fig. 4. Quantitative evaluation of struts thickness and pores size of the scaffolds before soaking in SBF: colour maps of the wall thickness distribution in the GC-BG scaffold (a) and in the GC-CEL2 scaffold (b); colour maps of the pore thickness distribution in the GC-BG scaffold (c) and in the GC-CEL2 scaffold (d); histograms of the wall thickness distribution (e) and of the pore thickness distribution (f) in the GC-BG and GC-CEL2 scaffolds, respectively (for sale of clearness, the distributions are reported as percentages upon the total struts/pores amount).
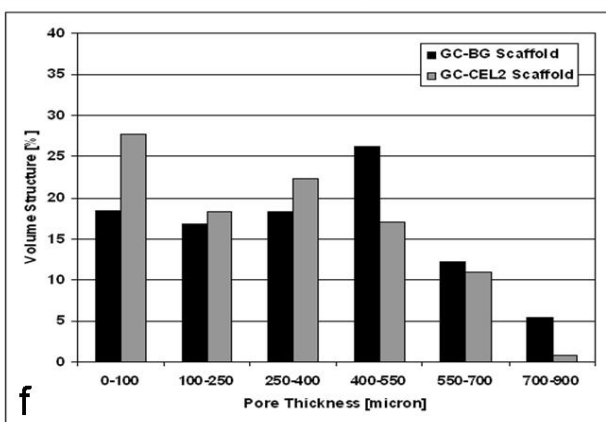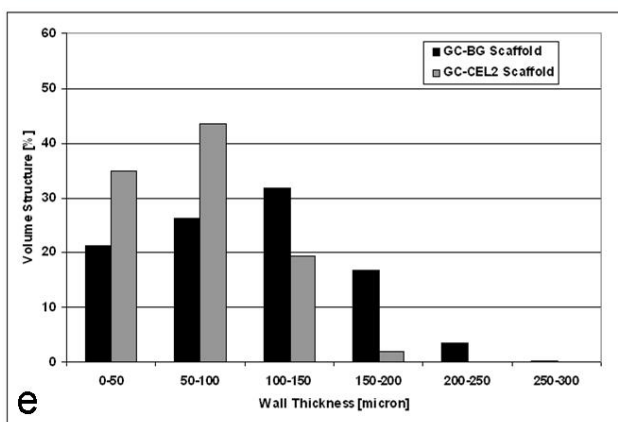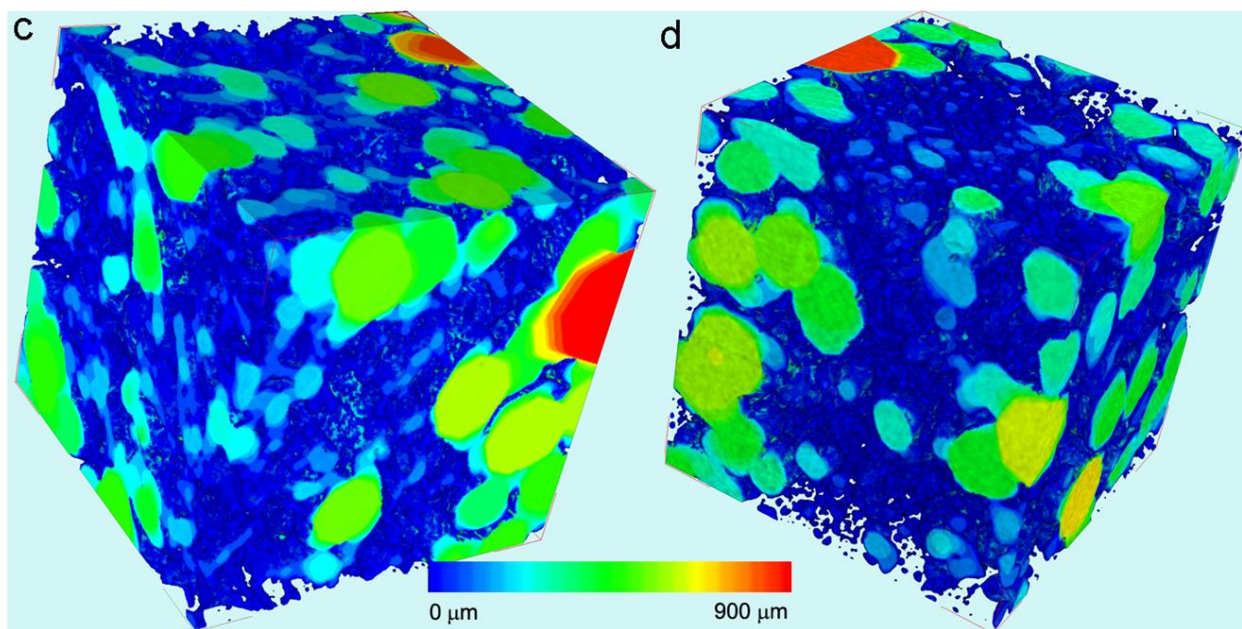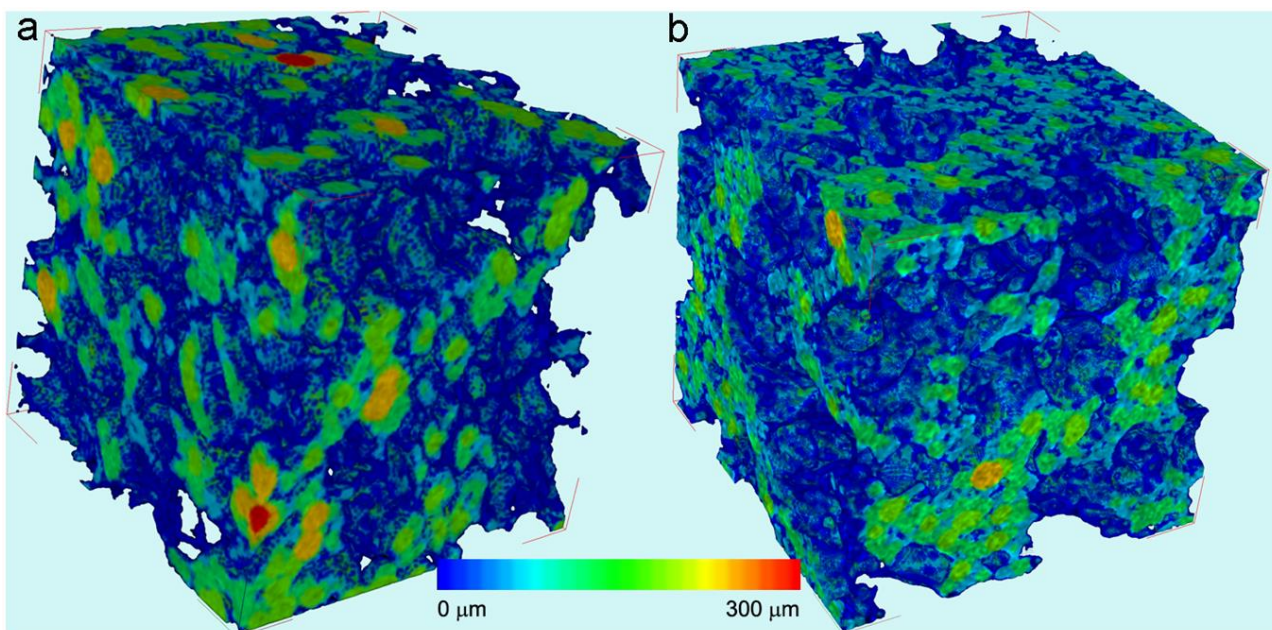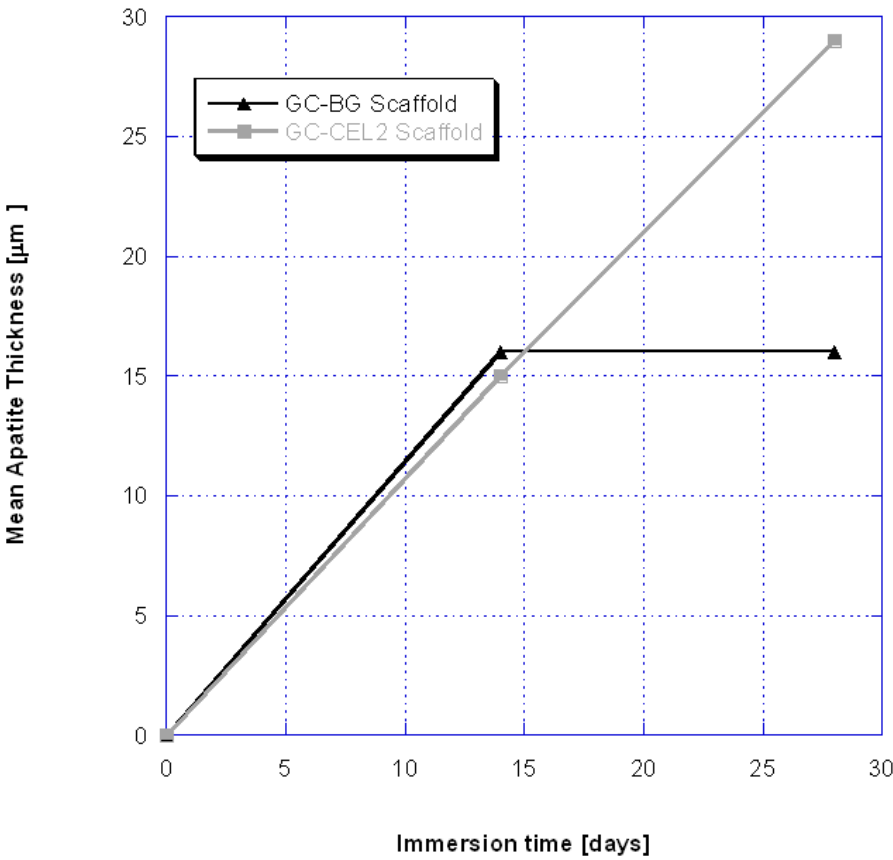
Fig. 5. SEM analysis after soaking for 28 days in SBF: HA formation on the struts of (a) GC-BG and (b) GC-CEL2 scaffold (magnification 400× in both cases); (c) typical "cauliflower" morphology of the HA grown on the scaffolds (magnification 7000×).
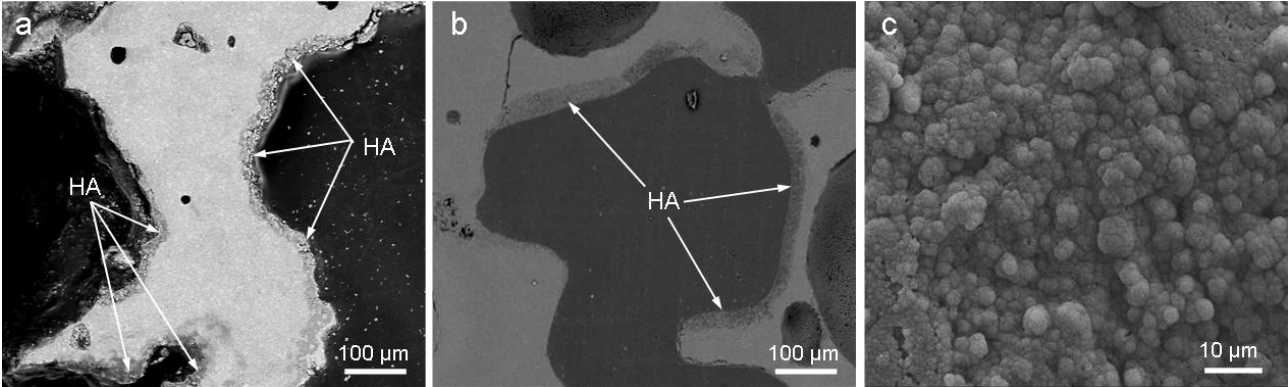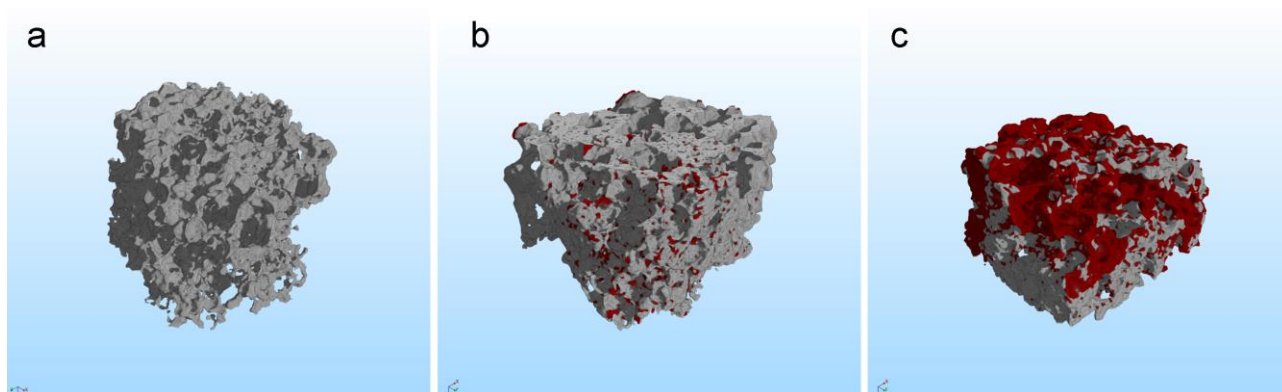

Fig. 6. Evolution of the mean thickness of the newly formed apatite layer as a function of soaking time.

Fig. 7. Volume rendering of a GC-BG scaffold subvolume before treatment (a) and after treatment in SBF for 2 weeks (b) and 4 weeks (c). The images show the scaffold material (gray) and the newly formed apatitic phase (red).


Fig. 8. Volume rendering of a GC-CEL2 scaffold subvolume before treatment (a) and after treatment in SBF for 2 weeks (b) and 4 weeks (b). The images show the scaffold material (gray) and the newly formed apatitic phase (red).
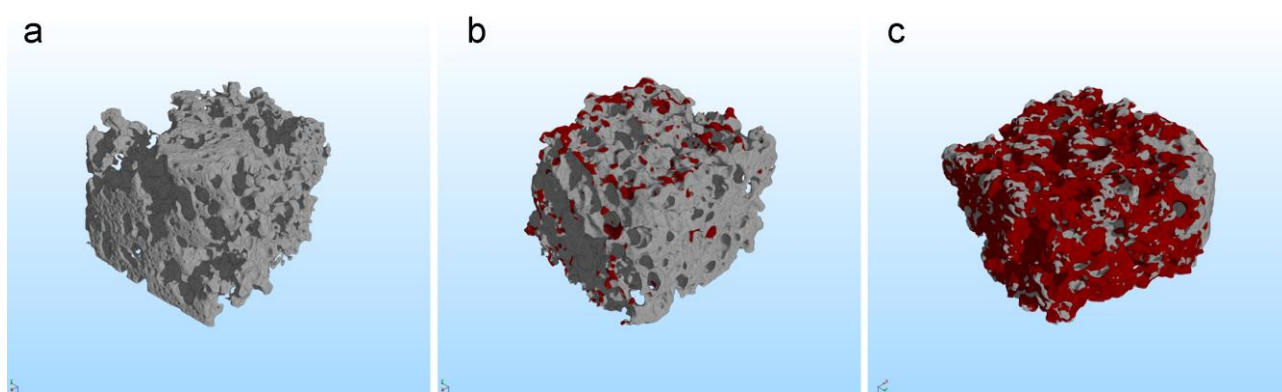
Fig. 9. Histograms of the pore size distribution, before and after treatment in SBF, for GC-BG scaffolds (a) and GC-CEL2 scaffolds (b) (for sake of clearness, the pores size distributions are reported as percentages upon the total pores amount).
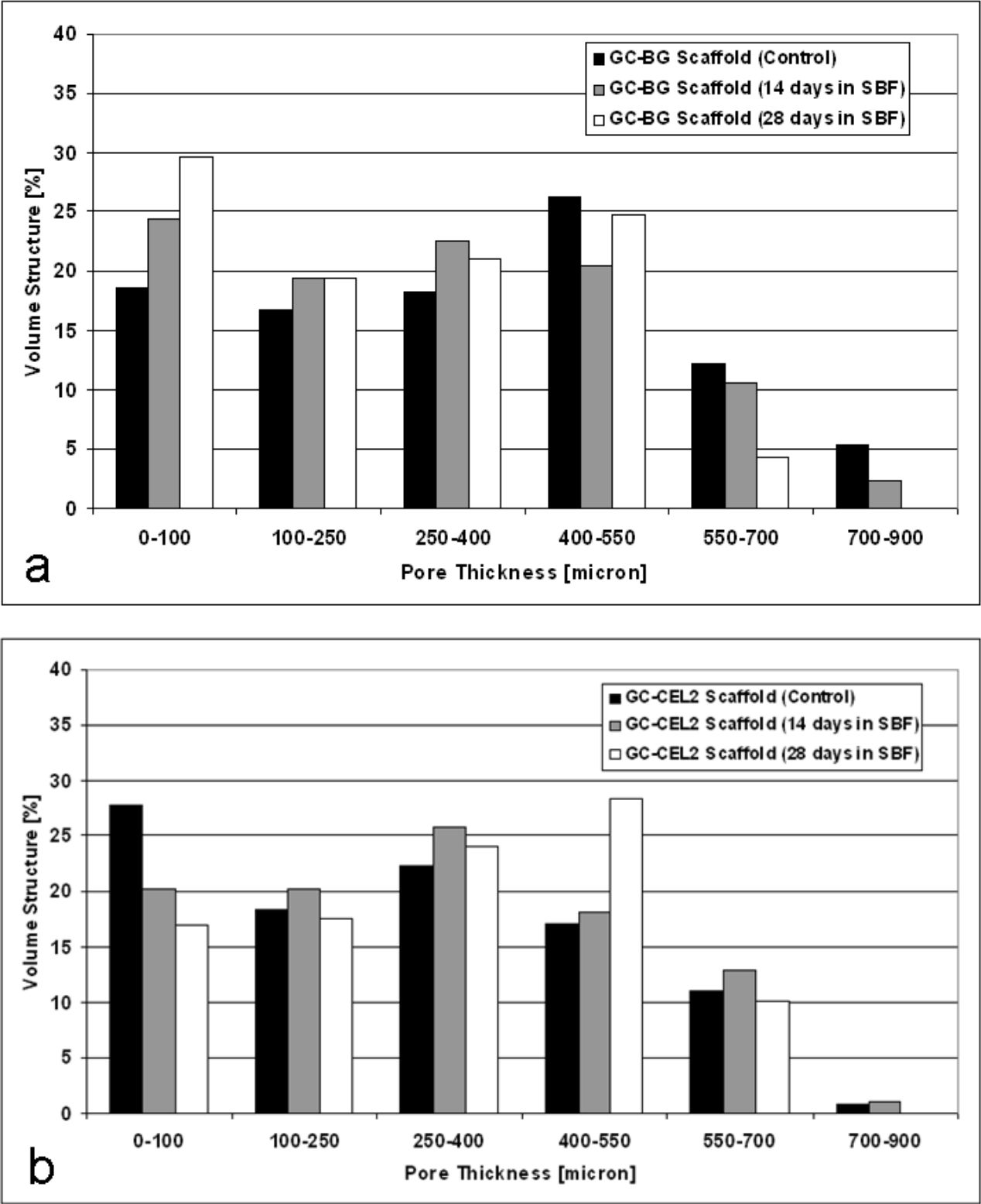
Fig. 10. Histograms of the struts thickness distribution, before and after treatment in SBF, for GC-BG scaffolds (a) and GC-CEL2 scaffolds (b) (for sake of clearness, the struts thickness distributions are reported as percentages upon the total struts amount).
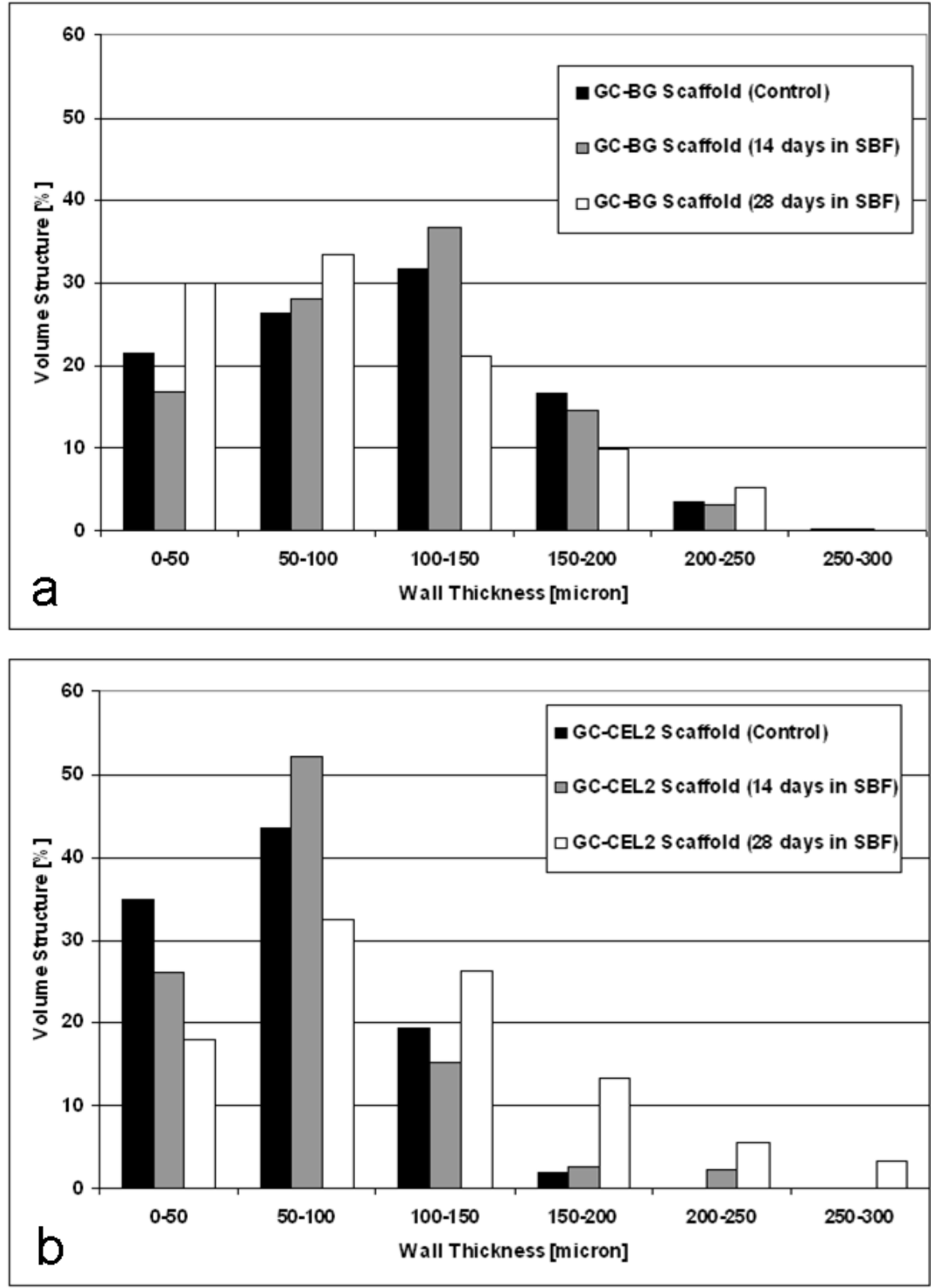
Tables

Table 1. Compositions and synthesis conditions of the starting glasses.

Glass	Composition (mol.%)						Raw products	Melting conditions
	SiO_2	P_2O_5	CaO	Na_2O	MgO	K_2O		
BG	46.1	2.6	26.9	24.4	-	-	SiO_2, $Ca_3(PO_4)_2$, $CaCO_3$, Na_2CO_3	1,500 °C for 1 h (heating rate: 10 °C min^{-1})
CEL2	45.0	3.0	26.0	15.0	7.0	4.0	SiO_2, $Ca_3(PO_4)_2$, $CaCO_3$, Na_2CO_3, $(MgCO_3)_4 \cdot Mg(OH)_2 \cdot 5H_2O$, K_2CO_3	1,400 °C for 1 h (heating rate: 10 °C min^{-1})

Table 2. 3-D quantitative analysis of the studied scaffolds before and after the treatments in SBF.

Samples	Soaking time in SBF (days)	PoreV (vol.%)	SS/SV (μm^{-1})
GC-BG scaffold	-	63.1	0.023
	14	43.1	0.015
	28	47.2	0.020
GC-CEL2 scaffold	-	40.2	0.015
	14	49.3	0.014
	28	42.6	0.011

Table 3. 3-D anisotropy analysis of the studied scaffolds before and after the treatments in SBF.

Samples	Soaking time in SBF (days)	Isotropy index, I (-)	Elongation index, E (-)
GC-BG scaffold	-	0.82	0.07
	14	0.89	0.06
	28	0.84	0.09
GC-CEL2 scaffold	-	0.86	0.09
	14	0.88	0.07
	28	0.86	0.09

Table 4. 3-D connectivity analysis of the studied scaffolds before and after the treatments in SBF.

Samples	Soaking time in SBF (days)	Connectivity index, β (mm^{-3})
GC-BG scaffold	-	3.97
	14	0.30
	28	0.91
GC-CEL2 scaffold	-	0.35
	14	1.31
	28	0.56